iScience

CellPress
OPEN ACCESS

Article

Trifluoperazine regulates blood-brain barrier permeability via the MLCK/p-MLC pathway to promote ischemic stroke recovery

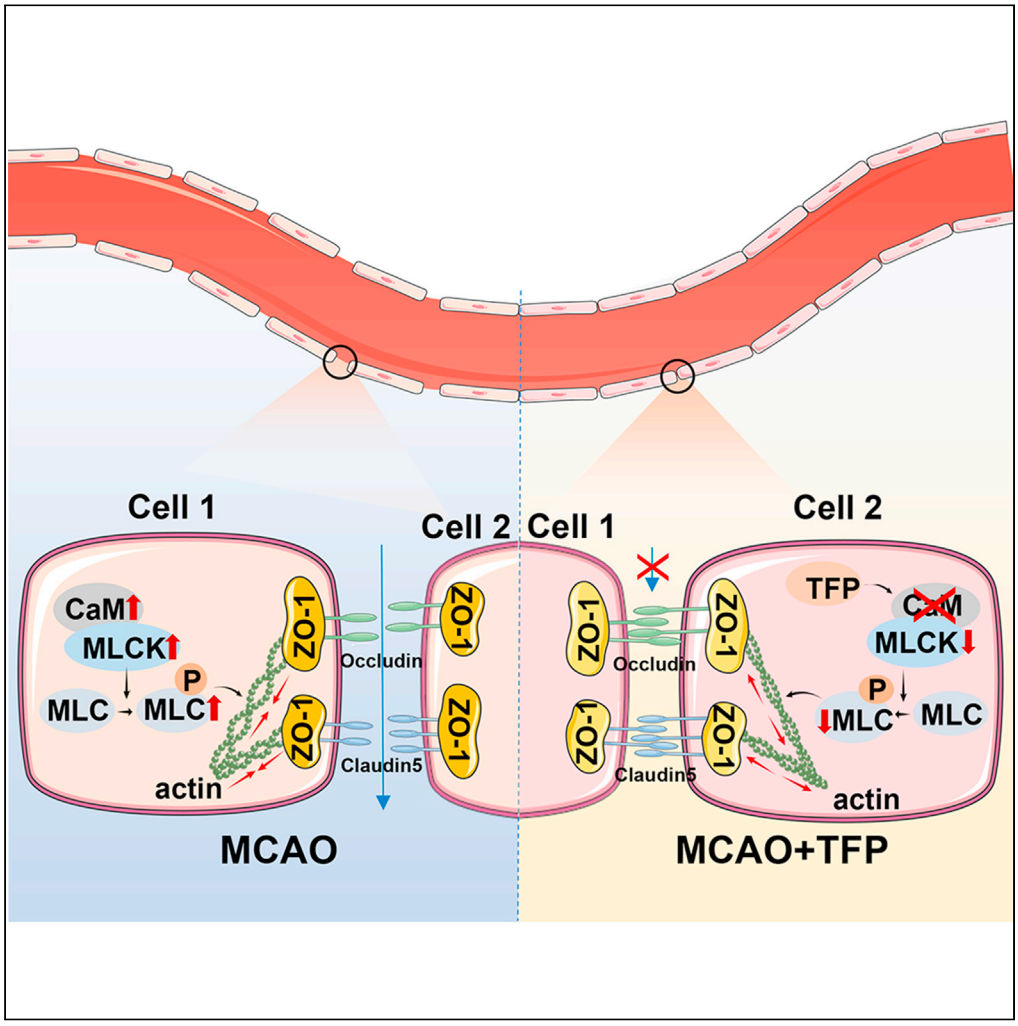

Wentao Zhang, Sisi Chen, Bin Ma, ..., Caijun He, Biao Wang, Mei Yuan

2012020002@usc.edu.cn

Highlights

The CaM level in the brain tissue of MCAO mice exhibited an elevation

Elevated CaM levels lead to the disruption of the BBB

TFP enhances BBB integrity through the CaM/MLCK/p-MLC pathway

Zhang et al., iScience 27, 109156
March 15, 2024
https://doi.org/10.1016/j.isci.2024.109156

iScience

CellPress
OPEN ACCESS

Article

Trifluoperazine regulates blood-brain barrier permeability via the MLCK/p-MLC pathway to promote ischemic stroke recovery

Wentao Zhang,[1] Sisi Chen,[1] Bin Ma,[1] Yingmei Ding,[1] Xiaofen Liu,[1] Caijun He,[1] Biao Wang,[1] and Mei Yuan[1,2,3,*]

SUMMARY

Blood-brain barrier (BBB) disruption following ischemic stroke (IS) can induce significant aftereffects. Elevated calmodulin (CaM) expression following stroke causes calcium overload—a key contributor to BBB collapse. Trifluoperazine (TFP), a CaM inhibitor, reduces CaM overexpression following IS. However, it remains unclear whether TFP participates in BBB repair after IS. We administered TFP to mice subjected to middle cerebral artery occlusion (MCAO) and bEnd.3 cells subjected to oxygen-glucose deprivation (OGD). TFP treatment in MCAO mice reduced cerebral CaM expression and infarct size and decreased BBB permeability. OGD-treated bEnd.3 cells showed significantly increased CaM protein levels and reduced tight junction (TJ) protein levels; these changes were reversed by TFP treatment. Our results found that TFP administration in mice inhibited actin contraction following cerebral ischemia-reperfusion by suppressing the MLCK/p-MLC pathway, thereby attenuating cell retraction, improving TJ protein integrity, and reducing BBB permeability. Consequently, this treatment may promote neurological function recovery after IS.

INTRODUCTION

Stroke is the third major cause of death and disabilities worldwide.[1] Stroke includes both the ischemic and hemorrhagic phenotypes. Approximately 85% of strokes are ischemic.[2] As the most common phenotype of stroke, ischemic stroke (IS) has significant mortality, morbidity, and recurrence rates and a limited recovery rate,[3,4] which makes the development of effective treatments for IS an urgent matter. Most cases of IS (~80%) involve the middle cerebral artery (MCA) region,[5] so animal models of stroke usually focus on the MCA territory. Numerous studies have recently been conducted on MCA occlusion (MCAO), and the treatment of MCAO is an important topic in the field of neurological research.

Acute cerebral ischemia has been suggested to increase vascular permeability and promote blood-brain barrier (BBB) disruption,[6] which is a key feature of IS.[7] **The BBB is formed by a complex network of endothelial cells (ECs), tight-junction (TJ) proteins, pericytes, astrocyte processes, and basal membranes. These constituents play a crucial role in establishing an optimal microenvironment. These constituents are essential to establish a suitable microenvironment.**[8] The BBB is vital for maintaining the normal functions of the cerebral and nervous systems. Major disability and poor clinical prognosis are associated with BBB disruption and the consequent cerebral edema that occurs in IS.[9] The exact mechanisms underlying the early increase in BBB permeability after cerebral ischemia/reperfusion (I/R) remain unclear. It has been suggested that the initial BBB penetration can be partly reversed,[10–12] which is considered a logical goal for the treatment of IS, particularly, during post-ischemic reperfusion. Ischemic cerebral infarction involves complex pathophysiological processes, including cellular calcium overabundance, energetic collapse, ion imbalance, inflammatory cellular damage, and glial cell activation, which ultimately lead to neural apoptosis or necrosis.[13]

Calcium overload is an important part of I/R injury and plays a critical role in calmodulin (CaM)-mediated ischemic brain injury.[14] Calcium ions (Ca^{2+}) are considered to be a major determinant of the functions of the BBB, **TJ proteins**, cytoskeleton, and extracellular matrix, which are all affected by Ca^{2+}-dependent pathways.[15] CaM is a multipurpose second messenger protein that mediates calcium transduction by coupling to Ca^{2+}.[16] In a rat model of I/R injury, CaM activity was observed to be increased in brain tissues.[17] Trifluoperazine (TFP) is a CaM inhibitor that belongs to the phenothiazine group.[18] A recent study reported that the inhibition of CaM with TFP prevented aquaporin 4 (AQP4) from localizing to the blood-spinal cord barrier, thereby reducing central nervous system edema and promoting functional recovery in rats.[19]

The objective of this study was to determine the efficacy of TFP in models of MCAO and reperfusion as well as elucidate its underlying biological mechanisms. We hypothesized that the MCAO model mice would have increased vascular permeability, BBB disruption, and increased CaM levels and that intervention with the CaM-specific inhibitor TFP would improve BBB permeability and restore motor function.

[1]The Second Affiliated Hospital, Department of Neurology, Hengyang Medical School, University of South China, Hengyang, Hunan 421001, China
[2]Affiliated Nanhua Hospital, Department of Neurology, Hengyang Medical School, University of South China, Hengyang, Hunan 421001, China
[3]Lead contact
*Correspondence: 2012020002@usc.edu.cn
https://doi.org/10.1016/j.isci.2024.109156

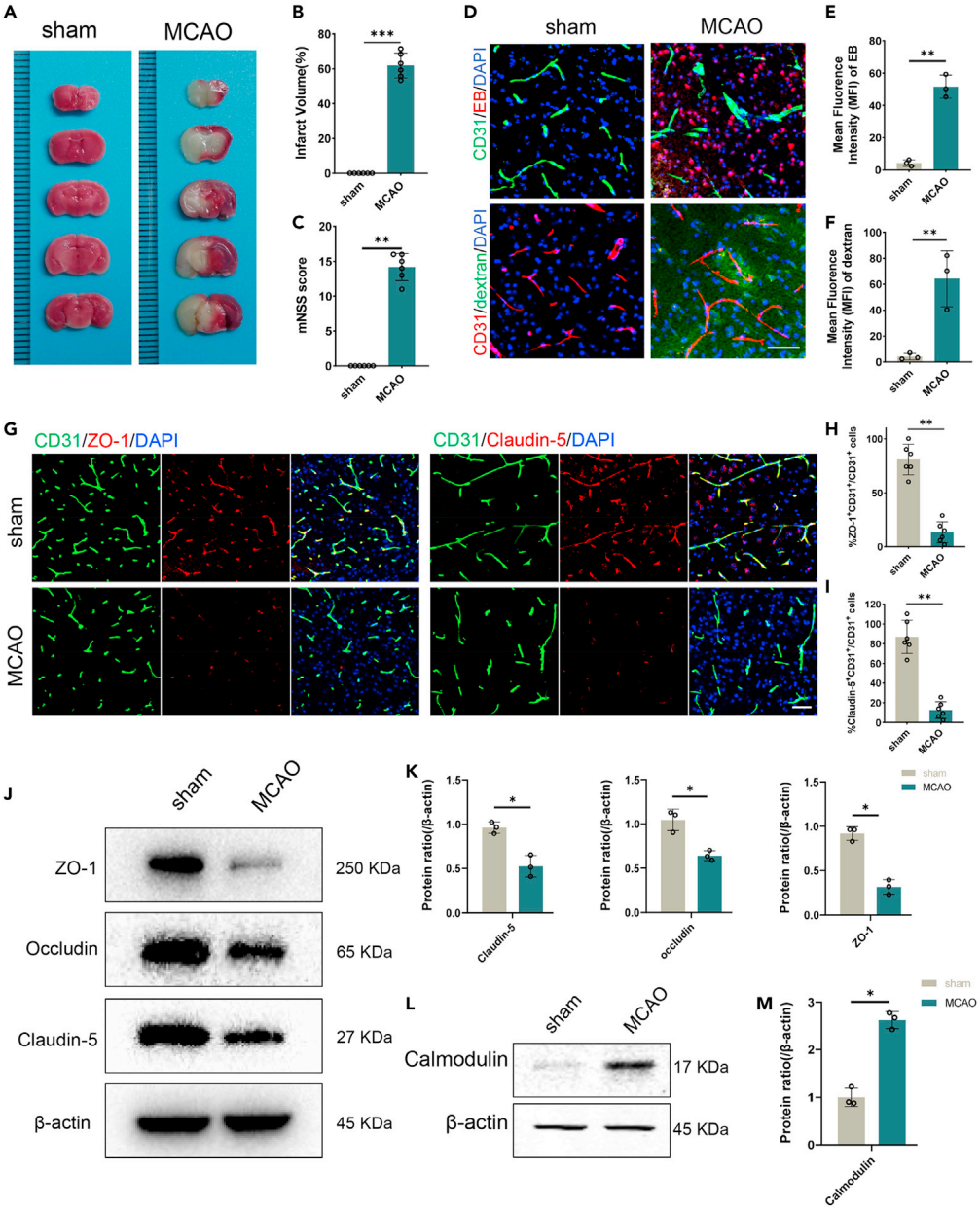

Figure 1. BBB permeability and CaM expression are both increased after MCAO in mice

(A) Representative mean fluorescent intensity of brain sections stained with TTC one day after MCAO.

(B) Infarct volume (n = 6).

(C) mNSS score (n = 6).

(D) Representative immunofluorescence pattern of ischemic brain samples from EB and FITC-dextran leakage tests taken before and after I/R in WT mice (scale bar, 50 μm).

(E and F) Quantitative analysis of the radiant efficiency of EB and FITC-dextran in (D) (n = 3 per group).

(G) Representative immunofluorescence images of ZO-1 or claudin-5 (red), CD31 (green), and DAPI (blue) staining of ischemic and normal brain areas in WT mice after I/R (scale bars, 50 μm).

(H and I) Quantitative analysis of $CD31^{+}ZO\text{-}1^{+}$ and $CD31^{+}claudin\text{-}5^{+}$ cells as a percentage of $CD31^{+}$ cells (n = 6 per group).

(J) Western blotting analysis of the levels of the TJ-related proteins ZO-1, occludin, and claudin-5 in WT mice before and after I/R.

(K) Quantitative analysis of the expression levels of ZO-1, occludin, and claudin-5 in (J) (n = 3 per group).

(L) Western blotting analysis of CaM protein expression levels in WT mice before and after I/R.

(M) Quantitative analysis of the expression levels of CaM in (L) (n = 3 per group). Data are represented as mean ± SEM. *p < 0.05, **p < 0.01.

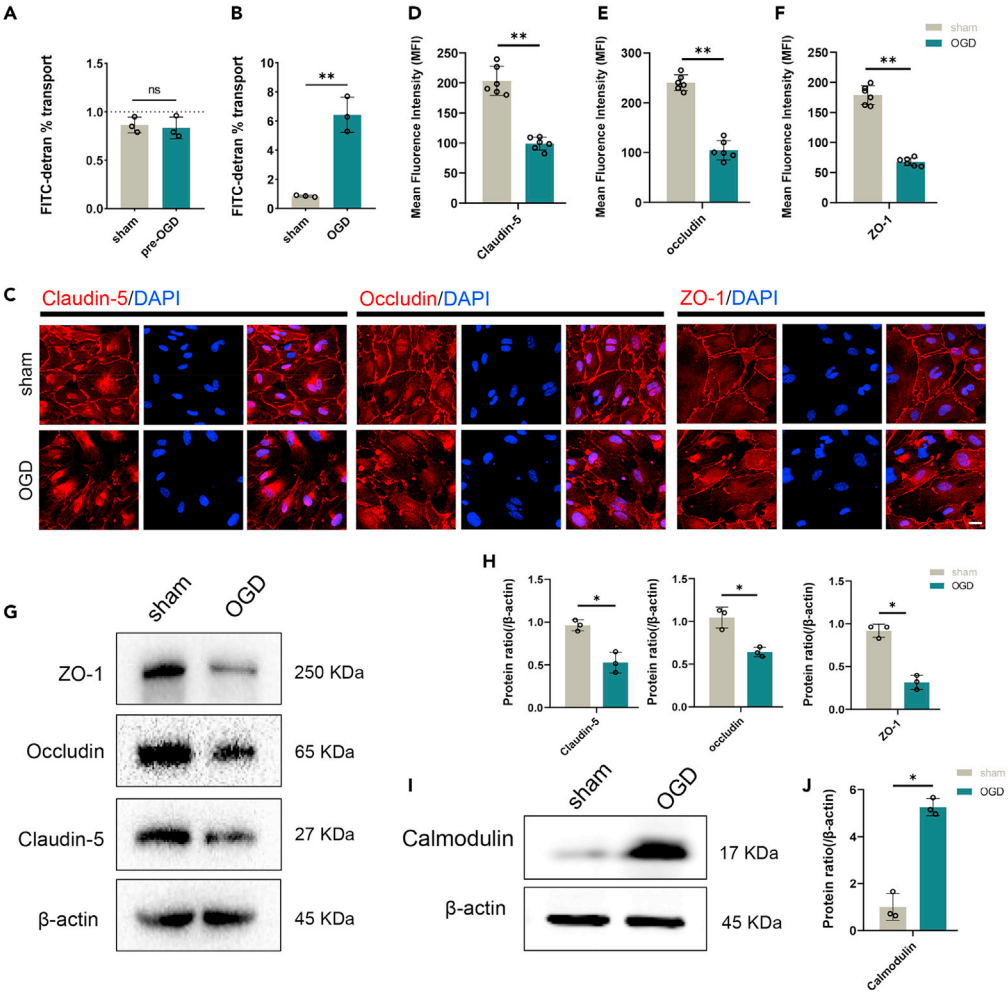

Figure 2. EC permeability and CaM expression are both increased after OGD in bEnd.3 cells

(A and B) FITC-dextran transport assay showing the permeability of bEnd.3 cells before and after OGD (n = 3 per group).

(C) Representative immunofluorescence images of TJ proteins (claudin-5, occludin, and ZO-1) in bEnd.3 cells after OGD (scale bar, 20 μm).

(D–F) Quantitative evaluation of the fluorescence intensity of claudin-5, occludin, and ZO-1 in (C) (n = 6 per group).

(G) Western blotting analysis of the levels of the TJ proteins ZO-1, occludin, and claudin-5 in WT mice after OGD.

(H) Quantitative analysis of the expression levels of ZO-1, occludin, and claudin-5 in (F) (n = 3 per group).

(I) Western blotting analysis of the CaM protein expression levels in bEnd.3 cells before and after OGD.

(J) Quantitative analysis of the expression levels of CaM in (I). Data are represented as mean ± SEM. *$p < 0.05$, **$p < 0.01$.

We also conducted experiments to determine the mechanisms underlying the aforementioned changes. We hope that the results of the current study will provide a theoretical basis that drives the development of potential clinical treatments for IS.

RESULTS

BBB permeability and CaM expression both increased after MCAO in mice

The MCAO model mice exhibited a significant increase in neurological deficit scores and significant areas of infarction (Figures 1A–1C). To investigate possible changes in BBB permeability after transient cerebral ischemia, we analyzed BBB permeability in the MCAO model wild-type (WT) mice by using EB and dextran leakage tests. Comparison of the fluorescence intensity of EB leakage revealed that BBB permeability was increased in mice after I/R, as compared with the control mice; this finding was confirmed by measuring the fluorescence intensity of dextran leakage (Figures 1D–1F). We immunofluorescence-labeled ZO-1, claudin-5, and the EC marker CD31 in the ischemic penumbra and found that the number of ZO-$1^{+}$$CD31^{+}$ and claudin-$5^{+}$$CD31^{+}$ cells was substantially reduced after MCAO (Figures 1G–1I). Furthermore, the claudin-5, occludin, and ZO-1 expression levels were significantly downregulated after MCAO, as shown by the western blot analysis (Figures 1J and 1K). Additionally, western blotting revealed a significant increase in CaM expression in the brain samples of the mice following

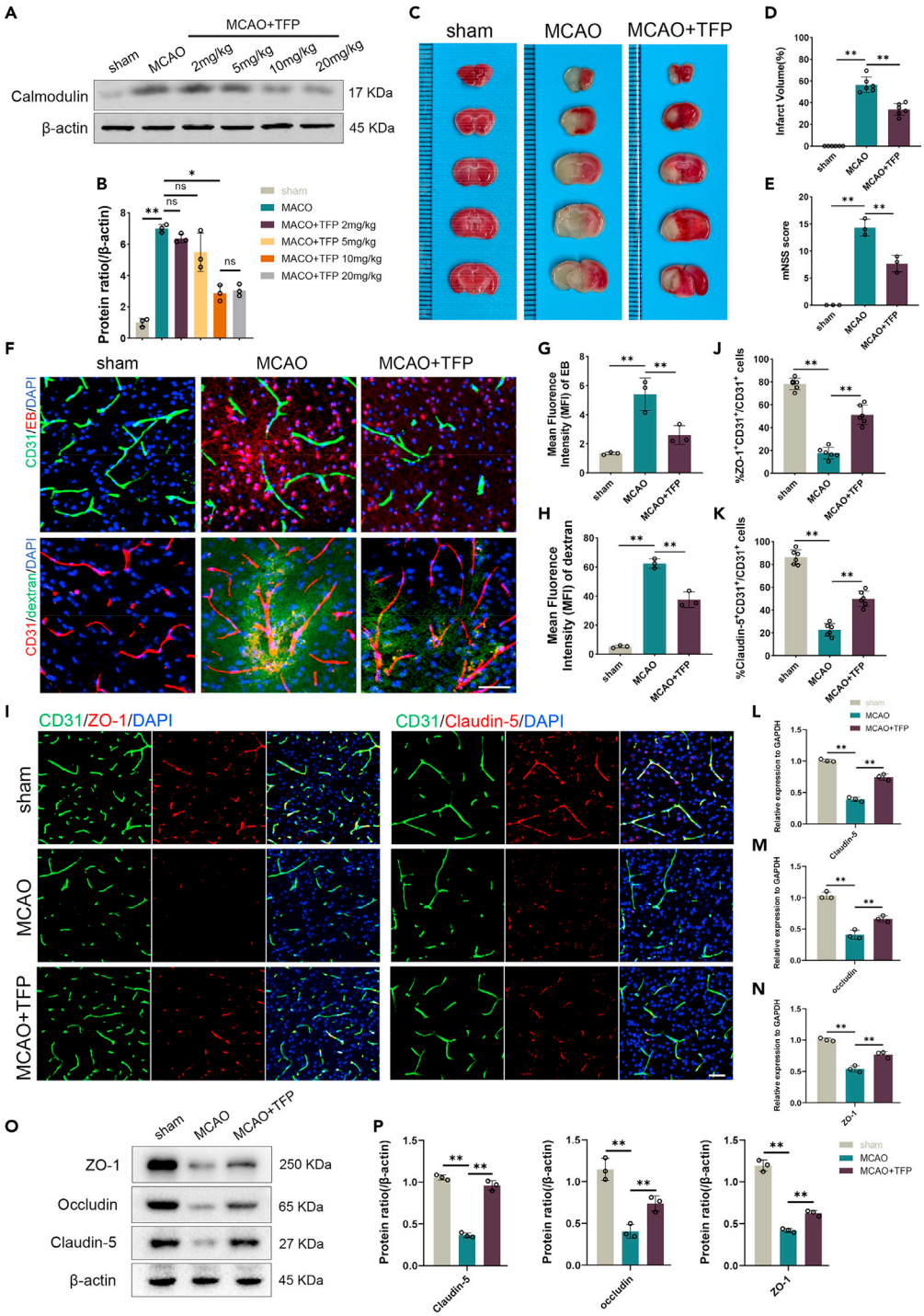

Figure 3. TFP reduces BBB disruption and improves stroke outcomes after IS

(A) Western blotting analysis of CaM protein expression levels in WT mice after I/R followed by treatment with TFP at different concentrations (2, 5, 10, and 20 mg/kg).

(B) Quantitative analysis of the expression levels of CaM in (A) (n = 3 per group).

(C) Representative brain sections stained with TTC.

(D) Infarct volume (n = 6).

(E) mNSS score (n = 6).

(F) Representative immunofluorescence images from EB-leakage tests taken before and after I/R followed by treatment with TFP in WT mice (scale bar, 50 mm).

Figure 3. *Continued*

(G and H) Quantitative analysis of the radiant efficiency of EB in (F) (n = 3 per group).

(I) Representative immunofluorescence images of ZO-1 or claudin-5 (red), CD31 (green), and DAPI (blue) staining of ischemic and normal brain areas in WT mice after I/R (scale bars, 50 μm).

(J and K) Quantitative analysis of $CD31^+ZO\text{-}1^+$ and $CD31^+claudin\text{-}5^+$ cells as a percentage of $CD31^+$ cells in (I) (n = 6 per group).

(L–N) RT-qPCR verification of the mRNA levels of claudin-5, occludin, and ZO-1 in WT mice after I/R followed by treatment with TFP (n = 3 per group).

(O) Western blotting analysis of ZO-1, occludin, and claudin-5 in WT mice after I/R followed by TFP treatment.

(P) Quantitative analysis of the expression levels of ZO-1, occludin, and claudin-5 in (O) (n = 3 per group). Data are represented as mean ± SEM. *$p < 0.05$, **$p < 0.01$.

I/R (Figures 1L and 1M). These results clearly demonstrate that I/R disrupted the TJs and increased BBB permeability and CaM expression. Therefore, we speculate that CaM is closely associated with BBB permeability after MCAO.

EC permeability and CaM expression both increased after OGD in bEnd.3 cells

ECs are the major structural element of the BBB and govern the integrity of the BBB. The bEnd.3 cell line was utilized to simulate the hypoxic-ischemic environment of vascular endothelial cells following ischemic stroke *in vivo* through OGD treatment. In accordance with previous literature,[20,21] we designed three distinct durations for OGD treatment: 2 h, 4 h, and 6 h. Our findings revealed that the cells exhibited a relatively impaired state after undergoing a 6-h OGD treatment. Therefore, we conducted a 4-h OGD treatment followed by a subsequent recovery period of 4 h under normal culture conditions. The addition of FITC-dextran for permeation experiments showed that before OGD, cell permeability was less than 1% in the two groups, without any significant differences among the groups (Figure 2A). After OGD, FITC-dextran permeability markedly increased in the OGD group (Figure 2B). In addition, the TJs were disrupted in the OGD group (Figures 2C–2F). Consistent results were found using western blot analysis (Figures 2G and 2H). In agreement with the findings in the ischemic brain samples, cells subjected to OGD exhibited an increase in CaM protein expression (Figures 2I and 2J). Collectively, the aforementioned data demonstrate the consistency of the *in vivo* and *in vitro* results.

TFP reduces BBB disruption and improves outcomes after MCAO in mice

As an antagonist of CaM,[22] TFP has been found to improve recovery from motor dysfunction and other impairments after MCAO.[18] Here, we treated MCAO mice with TFP to investigate its possible effects. To determine the optimal concentration of TFP, we measured the expression levels of CaM in mouse brain tissue samples after treatment with different doses of TFP (2, 5, 10, and 20 mg/kg; Figures 3A and 3B), based on the previously reported effects of TFP in rodents.[18,23,24] An equal volume of saline was given to the sham group. Ultimately, 10 mg/kg was chosen as the TFP dose. We assessed the level of brain damage in the MCAO mice after TFP treatment following IS. Compared with the MCAO group, the MCAO+TFP group showed significantly reduced infarct volumes and significantly improved neurological function (Figures 3C–3E). The immunofluorescence patterns showed that TFP significantly reduced EB and dextran extravasation in MCAO mice (Figures 3F–3H). Co-localization of TJ proteins with the EC marker CD31 was significantly reduced after MCAO; however, this co-localization was increased after the administration of TFP (Figures 3I–3K). Furthermore, the results of the RT-qPCR assays supported the aforementioned findings (Figures 3L–3N). Western blotting confirmed that the expressions of ZO-1, claudin-5, and occludin increased after TFP treatment, as compared with the MCAO group (Figures 3O and 3P). The aforementioned results indicate that TFP reduced BBB damage and improved neurological function after MCAO in mice.

TFP represses CaM expression levels and decreases BBB breakdown after OGD in bEnd.3 cells

To directly determine the effects of TFP treatment on endothelial integrity and barrier function, we treated bEnd.3 cells with TFP and used FITC-dextran for the bEnd.3 permeabilization experiments. The results showed that before OGD, cell permeability was less than 1% in all three groups, without any significant difference between the groups (Figure 4A). After OGD, the FITC-dextran permeability was significantly increased in both the OGD and OGD+TFP groups, but the increase was lower in the OGD+TFP group than in the OGD group (Figure 4B). We also examined the level of CaM expression after OGD. Consistent with the aforementioned *in vivo* experiment, CaM showed a decreasing trend after TFP treatment (Figures 4C and 4D). Immunofluorescence staining of claudin-5, occludin, and ZO-1 demonstrated that the fluorescence intensity of the TJs was significantly higher in the OGD+TFP group than in the OGD group (Figures 4E–4H). Furthermore, the results of the RT-qPCR (Figures 4I–4k) and the western blot assays (Figures 4L and 4M) supported the aforementioned findings. These results collectively suggest that TFP can decrease CaM expression and maintain the integrity of ECs.

MLCK plays a key role in the regulation of BBB permeability after MCAO

To further investigate the mechanism of BBB breakdown due to elevated CaM expression after MCAO, we reviewed the available literature and found that calcium overload after stroke leads to the activation of MLCK, which in turn causes BBB leakage.[15] MLCK is a CaM-dependent kinase.[25] We therefore investigated MLCK expression *in vivo* and *in vitro*. First, the immunofluorescence results showed that the expression of MLCK was significantly higher in the vascular endothelium in the MCAO group than in the control group, and after treatment with TFP, the vascular MLCK expression was significantly reduced (Figures 5A and 5B). These results were also confirmed in the cell studies. The *in vitro* MLCK level was significantly increased after OGD and decreased after TFP treatment (Figures 5C–5D). To investigate the impact of MLCK

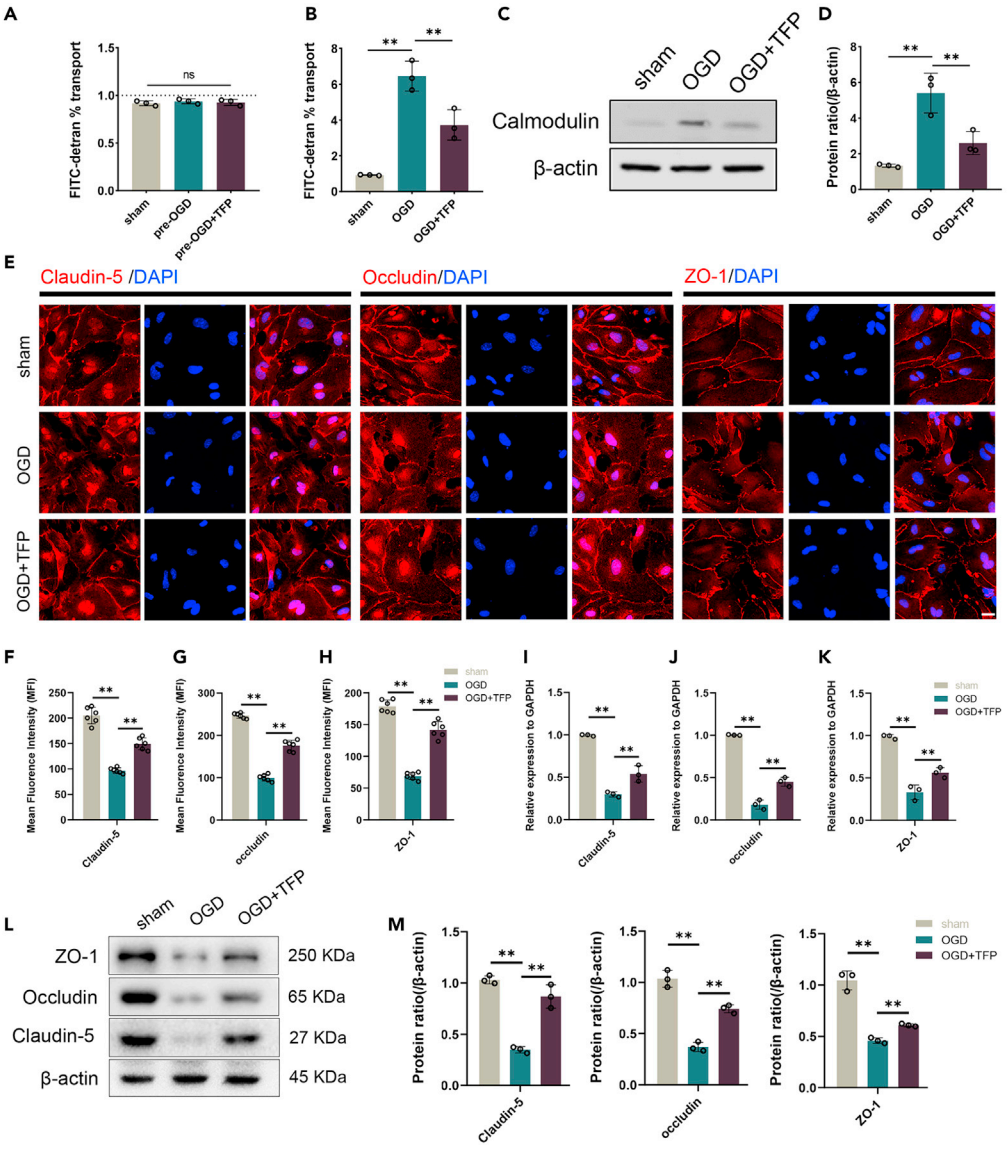

Figure 4. TFP represses CaM expression levels and decreases BBB breakdown after OGD

(A and B) FITC-dextran transport assay showing the permeability of bEnd.3 cells treated with TFP before and after OGD (n = 3 per group).

(C) Western blotting analysis of CaM protein expression levels in bEnd.3 cells treated with TFP after OGD.

(D) Quantitative analysis of the expression levels of CaM in (C) (n = 3 per group).

(E) Representative immunofluorescence images of TJ proteins (claudin-5, occludin, and ZO-1) in bEnd.3 cells subjected to OGD (scale bar, 20 μm).

(F–H) Quantitative evaluation of the fluorescence intensity of claudin-5, occludin, and ZO-1 in (E) (n = 6 per group).

(I–K) RT-qPCR verification of the mRNA levels of claudin-5, occludin, and ZO-1 in bEnd.3 cells after OGD followed by treatment with TFP (n = 3 per group).

(L) Western blotting analysis of ZO-1, occludin, and claudin-5 in bEnd.3 cells treated with TFP after OGD.

(M) Quantitative analysis of the expression levels of ZO-1, occludin, and claudin-5 in (L) (n = 3 per group). Data are represented as mean ± SEM. ns, $p > 0.05$, $^{**}p < 0.01$.

on BBB function, we utilized co-immunoprecipitation to detect the direct binding relationship between MLCK and CaM in brain tissue from MCAO mice. The results showed that MLCK could bind to CaM (Figure 5E), which is in line with the results of previous studies.[26] These results implicate MLCK as the key factor in BBB dysfunction after MCAO.

MLCK overexpression reverses the TFP-induced reduction in bEnd.3-cell permeability

To further confirm the MLCK-mediated regulation of BBB permeability after MCAO, we transfected bEnd.3 cells with an MLCK-overexpressing lentivirus and validated the transfection efficiency (Figures S1A and S1B). Before OGD, the cell permeability was below 1%, without any

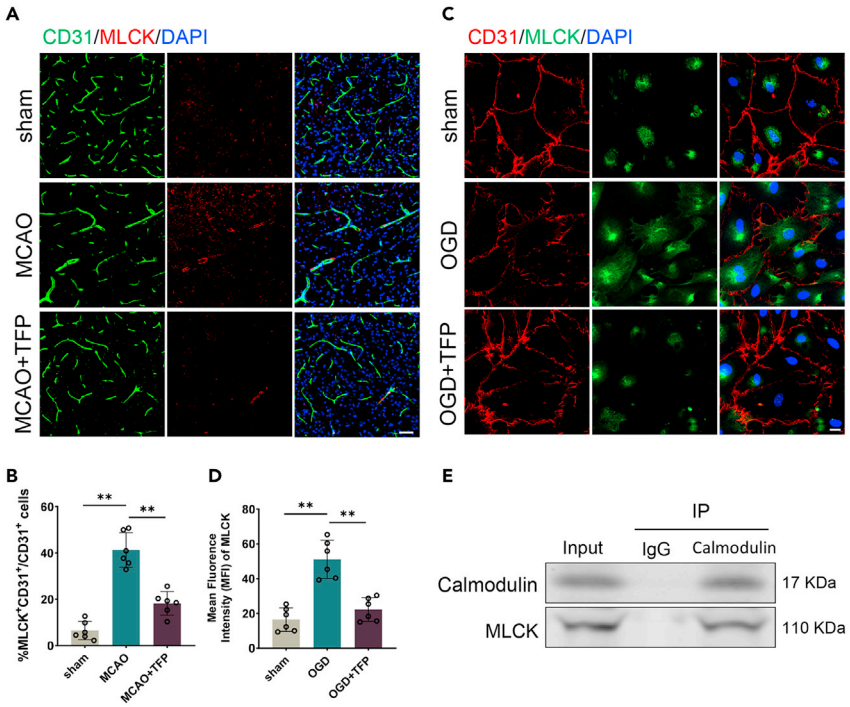

Figure 5. MLCK plays a key role in the regulation of BBB permeability after MCAO

(A) Representative immunofluorescence images of MLCK (red), CD31 (green), and DAPI (blue) staining of the mouse brain after MCAO followed by treatment with TFP (scale bars, 50 μm).

(B) Quantitative analysis of $CD31^+MLCK^+$ cells as a percentage of $CD31^+$ cells in (A) (n = 6 per group).

(C) Representative immunofluorescence images of MLCK (green), CD31 (red), and DAPI (blue) staining of bEnd.3 cells after OGD (scale bars, 20 μm).

(D) Quantitative analysis of the fluorescence intensity of MLCK in (C) (n = 6 per group).

(E) Brain tissue lysates from the indicated MCAO mice were immunoprecipitated with CaM antibody. The pellets were subjected to western blotting with antibodies against MLCK. Data are represented as mean ± SEM. ns, $p > 0.05$, *$p < 0.05$, **$p < 0.01$.

significant difference between the groups (Figure 6A). TFP treatment significantly reduced the permeability of bEnd.3 cells compared with the OGD group. However, the overexpression of MLCK counterbalanced this effect of TFP (Figure 6B). Immunofluorescence experiments revealed that the fluorescence intensities of claudin-5, occludin, and ZO-1 proteins were much higher in the OGD+TFP and OGD+TFP+control lentivirus groups than in the OGD+TFP+MLCK-overexpressing lentivirus group (Figures 6C–6F). We also measured the expression of TJ proteins by using western blot analysis. As expected, the expression levels of TJ proteins were increased after the overexpression of MLCK (Figures 6G and 6H). Together, these results suggest that MLCK is involved in the regulation of the intercellular permeability of bEnd.3 cells after OGD.

Overexpression of MLCK reversed the TFP-mediated reduction in BBB permeability in MCAO mice

To further test our hypothesis that MLCK reverses the TFP-induced reduction in BBB permeability in MCAO mice, we transfected the mice with an MLCK-overexpressing lentivirus and verified the transfection efficiency (Figures S1C and S1D). We administered the lentivirus four weeks before MCAO, assessed the BBB permeability after I/R, and performed neurological function examinations. We found that EB and FITC-dextran leakage were significantly lower in the TFP+control virus groups and significantly higher in the TFP+MLCK overexpression groups than in the MCAO group (Figures 7A–7C). The co-localization of ZO-1 and claudin-5 with CD31 was significantly reduced in the MLCK overexpression group as compared with the MCAO+TFP and MCAO+TFP+control virus groups and was at a similar level to the MCAO group (Figures 7D–7F). In addition, western blot analysis showed similar results (Figures 7G and 7H). The neurological scores in the *in vivo* experiments revealed that MLCK overexpression reversed the positive effects of TFP treatment (Figure 7I). These results suggest that MLCK is involved in regulating the altered vascular permeability after MCAO in mice.

TFP regulates BBB permeability via the MLCK/p-MLC signaling pathway and contributes to neurological recovery

MLCK is widespread in ECs and phosphorylates myosin light chain (MLC) in a Ca^{2+}-dependent manner.[27–29] MLCK strictly regulates MLC phosphorylation levels and promotes actin contraction, cytoskeletal contraction, cytoplasmic contraction, and TJ separation by phosphorylating MLC, which is a conventional mechanism for disrupting the intercellular barrier.[30,31] Here, we also demonstrated how TFP regulates vascular permeability after BBB via the MLCK/p-MLC pathway. We performed western blot experiments on brain tissues from differently treated mice, and the results showed that the protein levels of MLCK and p-MLC were higher in the MCAO group and significantly lower

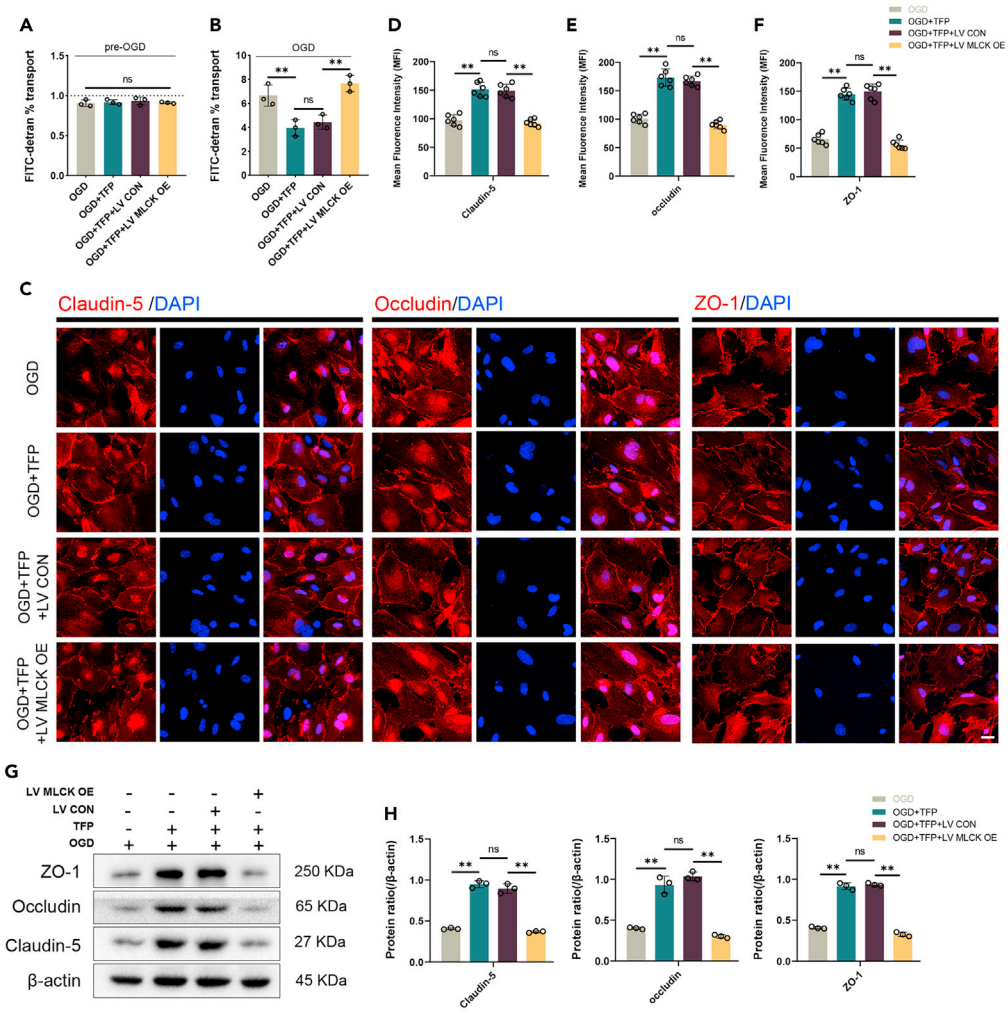

Figure 6. MLCK overexpression reverses the TFP-mediated reduction in the permeability of bEnd.3 cells

(A and B) FITC-dextran transport assay showing the permeability of bEnd.3 cells in the OGD, OGD+TFP, OGD+TFP+LV CON, and OGD+TFP+LV MLCK-OE groups before and after OGD (n = 3 per group).

(C) Representative immunofluorescence images of TJ proteins (claudin-5, occludin, and ZO-1) in bEnd.3 cells in the OGD, OGD+TFP, OGD+TFP+LV CON, and OGD+TFP+LV MLCK-OE groups after exposure to OGD (scale bar, 20 μm).

(D–F) Quantitative evaluation of the fluorescence intensity of claudin-5, occludin, and ZO-1 in (C) (n = 6 per group).

(G) Western blotting analysis of ZO-1, occludin, and claudin-5 in bEnd.3 cells in the OGD, OGD+TFP, OGD+TFP+LV CON, and OGD+TFP+LV MLCK-OE groups.

(H) Quantitative analysis of the expression levels of ZO-1, occludin, and claudin-5 in (G) (n = 3 per group). Data are represented as mean ± SEM. ns, $p > 0.05$, **$p < 0.01$.

in the MCAO+TFP group than in the control group. The overexpression of MLCK significantly increased the levels of p-MLC (Figures 8A and B). The results of immunofluorescence analysis revealed that the overexpression of MLCK increased the fluorescence intensity of p-MLC in the ECs, indicating that TFP reduces the increased permeability of the BBB after MCAO by activating the MLCK/p-MLC signaling pathway (Figures 8C and 8D). The aforementioned findings collectively suggest that TFP regulates vascular permeability through the MLCK/p-MLC pathway and aids neurological recovery after MCAO.

DISCUSSION

The purpose of this study was to investigate the effects of TFP on BBB integrity after IS. In mice subjected to MCAO followed by reperfusion for 24 h, TFP treatment significantly reduced infarct size and BBB breakdown, as measured by the TTC, EB, and FITC-dextran permeation assays. To further confirm the MLCK-mediated regulation of BBB permeability after MCAO, we transfected bEnd.3 cells with an MLCK-overexpressing lentivirus, and the results validated the *in vivo* findings. As a unique microvascular structure in the brain, the BBB helps regulate the passage of materials between the blood and the brain and maintains a homeostatic microenvironment for appropriate neuronal function.[32] Following IS,

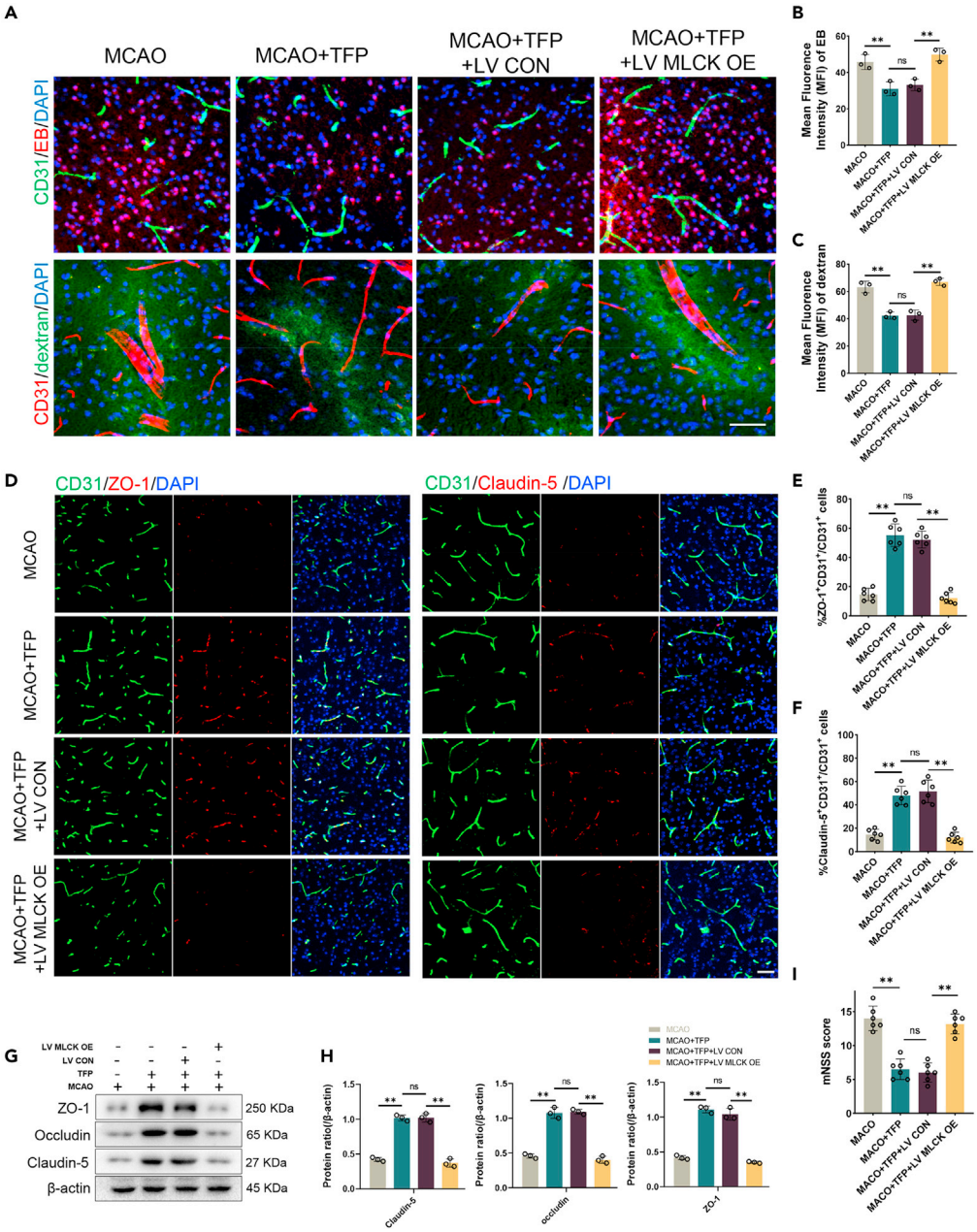

Figure 7. Overexpression of MLCK reversed the TFP-mediated reduction in BBB permeability in MCAO mice

(A) Representative immunofluorescence images of ischemic brain samples from the EB and FITC-dextran tests of mice in the MCAO, MCAO+TFP, MCAO+TFP+LV CON, and MCAO+TFP+LV MLCK-OE groups (scale bar, 50 μm).

(B and C) Quantitative analysis of the fluorescence intensity of EB and FITC-dextran in (A) (n = 3 per group).

(D) Representative immunofluorescence images of ZO-1 or claudin-5 (red), CD31 (green), and DAPI (blue) staining of the ischemic brain tissues of mice after I/R in the MCAO, MCAO+TFP, MCAO+TFP+LV CON, and MCAO+TFP+LV MLCK-OE groups (scale bars, 50 μm).

(E and F) Quantitative analysis of $CD31^{+}ZO\text{-}1^{+}$ and $CD31^{+}claudin\text{-}5^{+}$ cells as a percentage of $CD31^{+}$ cells in (D) (n = 6 per group).

(G) Western blotting analysis of the levels of the TJ-related proteins ZO-1, occludin, and claudin-5 in mice after I/R in the MCAO, MCAO+TFP, MCAO+TFP+LV CON, and MCAO+TFP+LV MLCK-OE groups.

(H) Quantitative analysis of the expression levels of ZO-1, occludin, and claudin-5 in (G) (n = 3 per group).

(I) mNSS score (n = 6 per group). Data are represented as mean ± SEM. ns, $p > 0.05$, *$p < 0.05$, **$p < 0.01$.

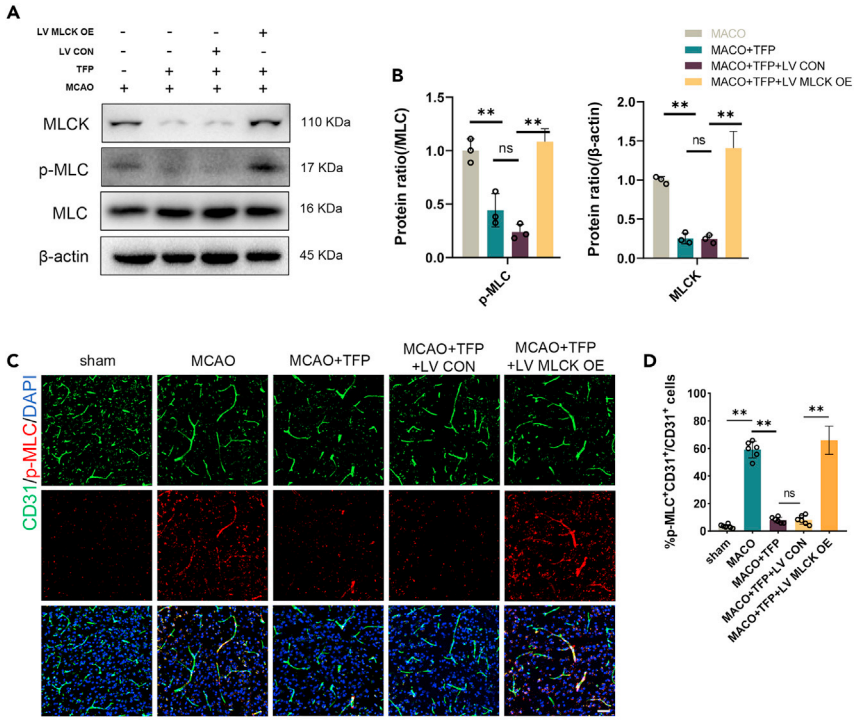

Figure 8. TFP regulates BBB permeability via the MLCK/p-MLC signaling pathway and contributes to neurological recovery

(A) Western blotting analysis of MLCK, p-MLC, and MLC in mice after I/R in the MCAO, MCAO+TFP, MCAO+TFP+LV CON, and MCAO+TFP+LV MLCK-OE groups.

(B) Quantitative analysis of the expression levels of MLCK and p-MLC in (A) (n = 3 per group).

(C) Representative immunofluorescence images of p-MLC (red), CD31 (green), and DAPI (blue) staining of mouse brain tissues after I/R in the sham, MCAO, MCAO+TFP, MCAO+TFP+LV CON, and MCAO+TFP+LV MLCK-OE groups (scale bars, 50 μm).

(D) Quantitative analysis of $CD31^{+}p\text{-}MLC^{+}$ cells as a percentage of $CD31^{+}$ cells in (D) (n = 6 per group). Data are represented as mean ± SEM. ns, $p > 0.05$, *$p < 0.05$, **$p < 0.01$.

the integrity of the BBB is compromised, which allows immune cells, pathogens, and harmful substances in the blood to enter the brain parenchyma more easily. This leads to a cascade of secondary injuries,[32] including vasogenic cerebral edema and hemorrhagic transformation, which may limit the use of tissue-type fibrinogen activator.[9,33] The current consensus is that the protection of BBB integrity in the early stages of IS after recanalization therapy is of great clinical value; however, there is virtually no clinically efficient treatment available to preserve the BBB. Therefore, preventing the disruption of the BBB following IS can be considered as an effective strategy for the clinical management of IS.

In WT mice subjected to 24 h of reperfusion after MCAO, TFP treatment significantly reduced infarct size and BBB breakdown, as measured by the TTC, EB, and FITC-dextran permeation assays. TFP is an inhibitor of CaM, one of the most important intracellular proteins for binding Ca^{2+}. Calcium overload is a major component of ischemic injury and plays an important role in the mechanism of CaM-mediated brain ischemia.[14] By altering the activity of Ca^{2+}-CaM-dependent protein kinase II, protein kinase C, phospholipase A2, proteases, nitric oxide synthase, calcineurin, and endonuclease, Ca^{2+}-CaM complexes trigger a cascade of tissue injuries.[18] Intercellular junctions and/or cytoskeletal proteins are the main targets of Ca^{2+}-activated signaling pathways. The balance between cell-cell adhesion and cytoskeletal contraction is essential for the regulation of BBB permeability. A perturbation of this balance is expected to enhance the diffusion of substances across the BBB. The endothelium of the BBB has zipper-like junctional complexes, consisting of TJs and adhesive junctions, which connect adjacent ECs and limit paracellular diffusion across the endothelium.[15] Our results suggest that TFP can rescue the TJ-protein loss caused by MCAO. Furthermore, these results were validated in an *in vitro* OGD model. In conclusion, our study provides important evidence that TFP protects BBB function and integrity after ischemia/hypoxia by inhibiting CaM expression and increasing TJ protein expression.

In subsequent experiments, we investigated the mechanism underlying the TFP-mediated inhibition of CaM expression that protects the functional integrity of the BBB after IS. The TJs between the ECs of the BBB limit the pathway for water-soluble compounds to diffuse from the blood into the brain. The BBB is an elaborate composite of transmembrane proteins (e.g., junctional adhesion molecule-1, occludin, and claudins) and cytoplasmic proteins (e.g., ZO-1, ZO-2, cingulin, AF-6, and 7H6) bound to the actin cytoskeleton.[34] The separation of the inter-EC junctions (such as TJ and adherent junction dissociation) and contraction of the EC cytoplasm, which are both dependent on the activity of EC molecular motor myosin II, are the main mechanisms driving the EC hyperpermeability response.[35,36] MLCK plays a crucial role in regulating the response of the vascular barrier to mechanical and inflammatory stimuli as well as in modulating EC permeability.[37,38] MLCK functions as a CaM-dependent kinase that triggers ATP-dependent actin contraction, cytoskeletal shrinkage, cytoplasmic retraction, and the disruption of

intercellular TJs (including occludin and claudins) through the phosphorylation of MLC.[39–41] The stabilization of ZO-1 at the TJs is linked to the regulation of vascular barrier function, and this regulation *in vivo* requires the action of MLCK, suggesting that MLCK-dependent ZO-1 exchange is critical for barrier-regulating mechanisms.[42] Tinsley et al. introduced MLCK into an *in vitro* model of a monolayer of coronary vein ECs and observed that MLCK significantly increased the phosphorylation level of MLC (approximately 60%), which was accompanied by an increase in the amount of albumin throughout the endothelium. After the addition of the MLCK inhibitor ML-9, the permeability of the ECs was reduced, and the cells adhered tightly again.[43] Hicks et al. also found that inhibiting MLCK with ML-7 can decrease the abnormal increase in the permeability of the BBB.[44]

Increasing evidence suggests that MLCK phosphorylates MLC in a calcium-dependent manner as a routine mechanism of TJ disruption.[15] The activation of MLCK by Ca^{2+} and CaM plays an important role in many cellular physiological functions. CaM-MLCK binding occurs as described here. Ca^{2+} enters the cytosol and binds to 4 Ca^{2+}-binding sites on CaM, which causes a dramatic conformational change in CaM.[45,46] CaM then binds to the CaM-binding region of MLCK, inducing a conformational change in MLCK that enables the activation of this kinase by displacing an autoinhibitory sequence from the catalytic domain of the kinase.[47] The study by MacEwen et al. supported the occurrence of CaM-MLCK binding by using mathematical modeling and biochemical analysis.[26] In the absence of Ca^{2+} or CaM, MLCK remains dormant because it is bound to its own pseudosubstrate domain, which has sequence homology to MLC, the physiological substrate. When CaM is present, this region is removed from the catalytic active position; the enzyme then actively phosphorylates itself.[48] The binding of MLCK to CaM was demonstrated in our study by means of co-immunoprecipitation. Based on these findings, we hypothesized that TFP regulates the permeability of the BBB via the MLCK/p-MLC pathway and promotes the recovery of neuronal functions. In subsequent experiments, we found that MLCK expression was significantly reduced in the MCAO model as compared with the sham group. Overexpressing MLCK by lentiviral transfection significantly reversed the beneficial effects of TFP on BBB protection and neurological function under hypoxic and ischemic conditions both *in vivo* and *in vitro*.

After MCAO, the BBB is disrupted, TJs are detached, and CaM is elevated. Our results suggest that after I/R, TFP regulates BBB permeability and TJ protein integrity via the CaM/MLCK/p-MLC pathway to improve stroke prognosis. Our findings suggest that the inhibition of CaM binding with MLCK by TFP holds promise as a therapeutic strategy for BBB injury following cerebral ischemia.

Limitations of the study

It should be acknowledged that there are certain limitations in this study. Our study revealed an upregulation of CaM expression and destruction of the BBB structure in MCAO mice, whereas TFP demonstrated its ability to protect the BBB in MCAO mice through the CaM/MLCK/p-MLC pathway. However, this study primarily focused on elucidating the pivotal role of MLCK in maintaining BBB integrity. Further investigation is warranted to explore whether TFP also safeguards BBB function after MCAO through alternative mechanisms.

STAR★METHODS

Detailed methods are provided in the online version of this paper and include the following:

- KEY RESOURCES TABLE
- RESOURCE AVAILABILITY
  - Lead contact
  - Materials availability
  - Data and code availability
- EXPERIMENTAL MODEL AND STUDY PARTICIPANT DETAILS
  - Animals
  - MCAO model mice and drug administration
  - Cell culture and reagents
- METHOD DETAILS
  - Measurement of infarct volume
  - Evans blue dye assays
  - Behavioral tests
  - Oxygen-glucose deprivation and reoxygenation
  - *In vitro* trans-endothelial permeability assay
  - Lentiviral transfection
  - Immunofluorescence assay
  - Western blotting
  - Co-immunoprecipitation assay
  - Quantitative real-time polymerase chain reaction assay
- QUANTIFICATION AND STATISTICAL ANALYSIS

SUPPLEMENTAL INFORMATION

Supplemental information can be found online at https://doi.org/10.1016/j.isci.2024.109156.

ACKNOWLEDGMENTS

This work was supported by the University of South China Clinical Research 4310 Program (20224310NHYCG08), the Natural Science Foundation of Hunan Province (2022JJ30523), the Health Research Project of Hunan Provincial Health Commission (202203072849), and the Clinical Medical Research Center of Hunan Province (2023SK4050). We thank the Medical Innovation Experimental Center of the Second Affiliated Hospital of the University of South China for providing the experimental conditions.

AUTHOR CONTRIBUTIONS

Conceptualization: M.Y. and W.T.Z.; methodology: W.T.Z., B.M., S.S.C., Y.M.D., and B.W.; investigation: W.T.Z., M.Y., X.F.C., and C.J.H.; visualization: W.T.Z.; supervision: M.Y.; writing—original draft: W.T.Z.; writing—review & editing: W.T.Z. and M.Y.

DECLARATION OF INTERESTS

The authors declare that there is no conflict of interest regarding the publication of this paper.

Received: September 18, 2023
Revised: December 19, 2023
Accepted: February 2, 2024
Published: February 13, 2024

REFERENCES

1. GBD 2019 Stroke Collaborators (2021). Global, regional, and national burden of stroke and its risk factors, 1990-2019: a systematic analysis for the Global Burden of Disease Study 2019. Lancet Neurol. *20*, 795–820. https://doi.org/10.1016/s1474-4422(21)00252-0.
2. Roger, V.L., Go, A.S., Lloyd-Jones, D.M., Adams, R.J., Berry, J.D., Brown, T.M., Carnethon, M.R., Dai, S., de Simone, G., Ford, E.S., et al. (2011). Heart disease and stroke statistics–2011 update: a report from the American Heart Association. Circulation *123*, e18–e209. https://doi.org/10.1161/CIR.0b013e3182009701.
3. Cerasuolo, J.O., Mandzia, J., Cipriano, L.E., Kapral, M.K., Fang, J., Hachinski, V., and Sposato, L.A. (2022). Intravenous Thrombolysis After First-Ever Ischemic Stroke and Reduced Incident Dementia Rate. Stroke *53*, 1170–1177. https://doi.org/10.1161/strokeaha.121.034969.
4. van den Berg, L.A., Berkhemer, O.A., Fransen, P.S.S., Beumer, D., Lingsma, H., Majoie, C.B.M., Dippel, D.W.J., van der Lugt, A., van Oostenbrugge, R.J., van Zwam, W.H., et al. (2022). Economic Evaluation of Endovascular Treatment for Acute Ischemic Stroke. Stroke *53*, 968–975. https://doi.org/10.1161/strokeaha.121.034599.
5. Suzuki, K., Matsumaru, Y., Takeuchi, M., Morimoto, M., Kanazawa, R., Takayama, Y., Kamiya, Y., Shigeta, K., Okubo, S., Hayakawa, M., et al. (2021). Effect of Mechanical Thrombectomy Without vs With Intravenous Thrombolysis on Functional Outcome Among Patients With Acute Ischemic Stroke: The SKIP Randomized Clinical Trial. JAMA *325*, 244–253. https://doi.org/10.1001/jama.2020.23522.
6. Yin, K.J., Deng, Z., Hamblin, M., Xiang, Y., Huang, H., Zhang, J., Jiang, X., Wang, Y., and Chen, Y.E. (2010). Peroxisome proliferator-activated receptor delta regulation of miR-15a in ischemia-induced cerebral vascular endothelial injury. J. Neurosci. *30*, 6398–6408. https://doi.org/10.1523/jneurosci.0780-10.2010.
7. Neuwelt, E.A., Bauer, B., Fahlke, C., Fricker, G., Iadecola, C., Janigro, D., Leybaert, L., Molnár, Z., O'Donnell, M.E., Povlishock, J.T., et al. (2011). Engaging neuroscience to advance translational research in brain barrier biology. Nat. Rev. Neurosci. *12*, 169–182. https://doi.org/10.1038/nrn2995.
8. Özen, I., Roth, M., Barbariga, M., Gaceb, A., Deierborg, T., Genové, G., and Paul, G. (2018). Loss of Regulator of G-Protein Signaling 5 Leads to Neurovascular Protection in Stroke. Stroke *49*, 2182–2190. https://doi.org/10.1161/strokeaha.118.020124.
9. Khatri, R., McKinney, A.M., Swenson, B., and Janardhan, V. (2012). Blood-brain barrier, reperfusion injury, and hemorrhagic transformation in acute ischemic stroke. Neurology *79*, S52–S57. https://doi.org/10.1212/WNL.0b013e3182697e70.
10. Neumann-Haefelin, T., Kastrup, A., de Crespigny, A., Yenari, M.A., Ringer, T., Sun, G.H., and Moseley, M.E. (2000). Serial MRI after transient focal cerebral ischemia in rats: dynamics of tissue injury, blood-brain barrier damage, and edema formation. Stroke *31*, 1965–1973. , discussion 1972-1963. https://doi.org/10.1161/01.str.31.8.1965.
11. Olah, L., Wecker, S., and Hoehn, M. (2000). Secondary deterioration of apparent diffusion coefficient after 1-hour transient focal cerebral ischemia in rats. J. Cerebr. Blood Flow Metabol. *20*, 1474–1482. https://doi.org/10.1097/00004647-200010000-00009.
12. Kaur, J., Tuor, U.I., Zhao, Z., Petersen, J., Jin, A.Y., and Barber, P.A. (2009). Quantified T1 as an adjunct to apparent diffusion coefficient for early infarct detection: a high-field magnetic resonance study in a rat stroke model. Int. J. Stroke *4*, 159–168. https://doi.org/10.1111/j.1747-4949.2009.00288.x.
13. Miao, Y., and Liao, J.K. (2014). Potential serum biomarkers in the pathophysiological processes of stroke. Expert Rev. Neurother. *14*, 173–185. https://doi.org/10.1586/14737175.2014.875471.
14. Moha Ou Maati, H., Widmann, C., Sedjelmaci, D., Gallois, B., Heurteaux, C., Borsotto, M., and Hugues, M. (2013). Mapacalcine protects mouse neurons against hypoxia by blocking cell calcium overload. PLoS One *8*, e66194. https://doi.org/10.1371/journal.pone.0066194.
15. De Bock, M., Wang, N., Decrock, E., Bol, M., Gadicherla, A.K., Culot, M., Cecchelli, R., Bultynck, G., and Leybaert, L. (2013). Endothelial calcium dynamics, connexin channels and blood-brain barrier function. Prog. Neurobiol. *108*, 1–20. https://doi.org/10.1016/j.pneurobio.2013.06.001.
16. Chin, D., and Means, A.R. (2000). Calmodulin: a prototypical calcium sensor. Trends Cell Biol. *10*, 322–328. https://doi.org/10.1016/s0962-8924(00)01800-6.
17. Tang, L.H., Xia, Z.Y., Zhao, B., Wei, X.D., Luo, T., and Meng, Q.T. (2011). Phosphocreatine preconditioning attenuates apoptosis in ischemia-reperfusion injury of rat brain. J. Biomed. Biotechnol. *2011*, 107091. https://doi.org/10.1155/2011/107091.
18. Kuroda, S., Nakai, A., Kristían, T., and Siesjö, B.K. (1997). The calmodulin antagonist trifluoperazine in transient focal brain ischemia in rats. Anti-ischemic effect and therapeutic window. Stroke *28*, 2539–2544. https://doi.org/10.1161/01.str.28.12.2539.
19. Kitchen, P., Salman, M.M., Halsey, A.M., Clarke-Bland, C., MacDonald, J.A., Ishida, H., Vogel, H.J., Almutiri, S., Logan, A., Kreida, S., et al. (2020). Targeting Aquaporin-4 Subcellular Localization to Treat Central Nervous System Edema. Cell *181*, 784–799.e19. https://doi.org/10.1016/j.cell.2020.03.037.
20. Wan, J.J., Wang, P.Y., Zhang, Y., Qin, Z., Sun, Y., Hu, B.H., Su, D.F., Xu, D.P., and Liu, X. (2019). Role of acute-phase protein ORM in a mice model of ischemic stroke. J. Cell. Physiol. *234*, 20533–20545. https://doi.org/10.1002/jcp.28653.
21. Ji, Y., Gao, Q., Ma, Y., Wang, F., Tan, X., Song, D., Hoo, R.L.C., Wang, Z., Ge, X., Han, H., et al. (2023). An MMP-9 exclusive neutralizing antibody attenuates blood-brain barrier breakdown in mice with stroke and reduces stroke patient-derived MMP-9 activity. Pharmacol. Res. *190*, 106720. https://doi.org/10.1016/j.phrs.2023.106720.
22. Vandonselaar, M., Hickie, R.A., Quail, J.W., and Delbaere, L.T. (1994). Trifluoperazine-induced conformational change in Ca(2+)-calmodulin. Nat. Struct. Biol. *1*, 795–801. https://doi.org/10.1038/nsb1194-795.

23. Kang, S., Hong, J., Lee, J.M., Moon, H.E., Jeon, B., Choi, J., Yoon, N.A., Paek, S.H., Roh, E.J., Lee, C.J., and Kang, S.S. (2017). Trifluoperazine, a Well-Known Antipsychotic, Inhibits Glioblastoma Invasion by Binding to Calmodulin and Disinhibiting Calcium Release Channel IP3R. Mol. Cancer Therapeut. *16*, 217–227. https://doi.org/10.1158/1535-7163.mct-16-0169-t.
24. Chaudhuri, S., McCullough, S.S., Hennings, L., Brown, A.T., Li, S.H., Simpson, P.M., Hinson, J.A., and James, L.P. (2012). Effect of trifluoperazine on toxicity, HIF-1α induction and hepatocyte regeneration in acetaminophen toxicity in mice. Toxicol. Appl. Pharmacol. *264*, 192–201. https://doi.org/10.1016/j.taap.2012.08.001.
25. Wang, L., and Shilatifard, A. (2019). UTX Mutations in Human Cancer. Cancer Cell *35*, 168–176. https://doi.org/10.1016/j.ccell.2019.01.001.
26. MacEwen, M.J.S., Rusnac, D.V., Ermias, H., Locke, T.M., Gizinski, H.E., Dexter, J.P., and Sancak, Y. (2023). Mathematical modeling and biochemical analysis support partially ordered calmodulin-myosin light chain kinase binding. iScience *26*, 106146. https://doi.org/10.1016/j.isci.2023.106146.
27. Garcia, J.G., Davis, H.W., and Patterson, C.E. (1995). Regulation of endothelial cell gap formation and barrier dysfunction: role of myosin light chain phosphorylation. J. Cell. Physiol. *163*, 510–522. https://doi.org/10.1002/jcp.1041630311.
28. Goeckeler, Z.M., and Wysolmerski, R.B. (1995). Myosin light chain kinase-regulated endothelial cell contraction: the relationship between isometric tension, actin polymerization, and myosin phosphorylation. J. Cell Biol. *130*, 613–627. https://doi.org/10.1083/jcb.130.3.613.
29. Verin, A.D., Gilbert-McClain, L.I., Patterson, C.E., and Garcia, J.G. (1998). Biochemical regulation of the nonmuscle myosin light chain kinase isoform in bovine endothelium. Am. J. Respir. Cell Mol. Biol. *19*, 767–776. https://doi.org/10.1165/ajrcmb.19.5.3126.
30. Fang, Z., Sun, X., Wang, X., Ma, J., Palaia, T., Rana, U., Miao, B., Ragolia, L., Hu, W., and Miao, Q.R. (2022). NOGOB receptor deficiency increases cerebrovascular permeability and hemorrhage via impairing histone acetylation-mediated CCM1/2 expression. J. Clin. Invest. *132*, e151382. https://doi.org/10.1172/jci151382.
31. Rigor, R.R., Shen, Q., Pivetti, C.D., Wu, M.H., and Yuan, S.Y. (2013). Myosin light chain kinase signaling in endothelial barrier dysfunction. Med. Res. Rev. *33*, 911–933. https://doi.org/10.1002/med.21270.
32. Obermeier, B., Daneman, R., and Ransohoff, R.M. (2013). Development, maintenance and disruption of the blood-brain barrier. Nat. Med. *19*, 1584–1596. https://doi.org/10.1038/nm.3407.
33. Moskowitz, M.A., Lo, E.H., and Iadecola, C. (2010). The science of stroke: mechanisms in search of treatments. Neuron *67*, 181–198. https://doi.org/10.1016/j.neuron.2010.07.002.
34. Hawkins, B.T., and Davis, T.P. (2005). The blood-brain barrier/neurovascular unit in health and disease. Pharmacol. Rev. *57*, 173–185. https://doi.org/10.1124/pr.57.2.4.
35. Lan, F., Bayliss, P.E., Rinn, J.L., Whetstine, J.R., Wang, J.K., Chen, S., Iwase, S., Alpatov, R., Issaeva, I., Canaani, E., et al. (2007). A histone H3 lysine 27 demethylase regulates animal posterior development. Nature *449*, 689–694. https://doi.org/10.1038/nature06192.
36. Shi, B., Li, W., Song, Y., Wang, Z., Ju, R., Ulman, A., Hu, J., Palomba, F., Zhao, Y., Le, J.P., et al. (2021). UTX condensation underlies its tumour-suppressive activity. Nature *597*, 726–731. https://doi.org/10.1038/s41586-021-03903-7.
37. Mascarenhas, J.B., Tchourbanov, A.Y., Fan, H., Danilov, S.M., Wang, T., and Garcia, J.G.N. (2017). Mechanical Stress and Single Nucleotide Variants Regulate Alternative Splicing of the MYLK Gene. Am. J. Respir. Cell Mol. Biol. *56*, 29–37. https://doi.org/10.1165/rcmb.2016-0053OC.
38. He, W.Q., Wang, J., Sheng, J.Y., Zha, J.M., Graham, W.V., and Turner, J.R. (2020). Contributions of Myosin Light Chain Kinase to Regulation of Epithelial Paracellular Permeability and Mucosal Homeostasis. Int. J. Mol. Sci. *21*, 993. https://doi.org/10.3390/ijms21030993.
39. Dong, L., Xie, J., Wang, Y., Jiang, H., Chen, K., Li, D., Wang, J., Liu, Y., He, J., Zhou, J., et al. (2022). Mannose ameliorates experimental colitis by protecting intestinal barrier integrity. Nat. Commun. *13*, 4804. https://doi.org/10.1038/s41467-022-32505-8.
40. Jiang, J., Huang, K., Xu, S., Garcia, J.G.N., Wang, C., and Cai, H. (2020). Targeting NOX4 alleviates sepsis-induced acute lung injury via attenuation of redox-sensitive activation of CaMKII/ERK1/2/MLCK and endothelial cell barrier dysfunction. Redox Biol. *36*, 101638. https://doi.org/10.1016/j.redox.2020.101638.
41. Izawa, Y., Gu, Y.H., Osada, T., Kanazawa, M., Hawkins, B.T., Koziol, J.A., Papayannopoulou, T., Spatz, M., and Del Zoppo, G.J. (2018). β1-integrin-matrix interactions modulate cerebral microvessel endothelial cell tight junction expression and permeability. J. Cerebr. Blood Flow Metabol. *38*, 641–658. https://doi.org/10.1177/0271678x17722108.
42. Yu, D., Marchiando, A.M., Weber, C.R., Raleigh, D.R., Wang, Y., Shen, L., and Turner, J.R. (2010). MLCK-dependent exchange and actin binding region-dependent anchoring of ZO-1 regulate tight junction barrier function. Proc. Natl. Acad. Sci. USA *107*, 8237–8241. https://doi.org/10.1073/pnas.0908869107.
43. Tinsley, J.H., De Lanerolle, P., Wilson, E., Ma, W., and Yuan, S.Y. (2000). Myosin light chain kinase transference induces myosin light chain activation and endothelial hyperpermeability. Am. J. Physiol. Cell Physiol. *279*, C1285–C1289. https://doi.org/10.1152/ajpcell.2000.279.4.C1285.
44. Hicks, K., O'Neil, R.G., Dubinsky, W.S., and Brown, R.C. (2010). TRPC-mediated actin-myosin contraction is critical for BBB disruption following hypoxic stress. Am. J. Physiol. Cell Physiol. *298*, C1583–C1593. https://doi.org/10.1152/ajpcell.00458.2009.
45. Xia, Z., and Storm, D.R. (2005). The role of calmodulin as a signal integrator for synaptic plasticity. Nat. Rev. Neurosci. *6*, 267–276. https://doi.org/10.1038/nrn1647.
46. Swulius, M.T., and Waxham, M.N. (2008). Ca(2+)/calmodulin-dependent protein kinases. Cell. Mol. Life Sci. *65*, 2637–2657. https://doi.org/10.1007/s00018-008-8086-2.
47. Park, H.Y., Kim, S.A., Korlach, J., Rhoades, E., Kwok, L.W., Zipfel, W.R., Waxham, M.N., Webb, W.W., and Pollack, L. (2008). Conformational changes of calmodulin upon Ca2+ binding studied with a microfluidic mixer. Proc. Natl. Acad. Sci. USA *105*, 542–547. https://doi.org/10.1073/pnas.0710810105.
48. Filenko, A.M., Danilova, V.M., and Sobieszek, A. (1997). Smooth muscle myosin light chain kinase, supramolecular organization, modulation of activity, and related conformational changes. Biophys. J. *73*, 1593–1606. https://doi.org/10.1016/s0006-3495(97)78191-8.
49. Zhou, Z., Xu, N., Matei, N., McBride, D.W., Ding, Y., Liang, H., Tang, J., and Zhang, J.H. (2021). Sodium butyrate attenuated neuronal apoptosis via GPR41/Gβγ/PI3K/Akt pathway after MCAO in rats. J. Cerebr. Blood Flow Metabol. *41*, 267–281. https://doi.org/10.1177/0271678x20910533.
50. Sylvain, N.J., Salman, M.M., Pushie, M.J., Hou, H., Meher, V., Herlo, R., Peeling, L., and Kelly, M.E. (2021). The effects of trifluoperazine on brain edema, aquaporin-4 expression and metabolic markers during the acute phase of stroke using photothrombotic mouse model. Biochim. Biophys. Acta Biomembr. *1863*, 183573. https://doi.org/10.1016/j.bbamem.2021.183573.
51. Hu, Q., Manaenko, A., Bian, H., Guo, Z., Huang, J.L., Guo, Z.N., Yang, P., Tang, J., and Zhang, J.H. (2017). Hyperbaric Oxygen Reduces Infarction Volume and Hemorrhagic Transformation Through ATP/NAD(+)/Sirt1 Pathway in Hyperglycemic Middle Cerebral Artery Occlusion Rats. Stroke *48*, 1655–1664. https://doi.org/10.1161/strokeaha.116.015753.
52. Chang, J., Mancuso, M.R., Maier, C., Liang, X., Yuki, K., Yang, L., Kwong, J.W., Wang, J., Rao, V., Vallon, M., et al. (2017). Gpr124 is essential for blood-brain barrier integrity in central nervous system disease. Nat. Med. *23*, 450–460. https://doi.org/10.1038/nm.4309.
53. Guo, C., Zhou, X., Wang, X., Wang, H., Liu, J., Wang, J., Lin, X., Lei, S., Yang, Y., Liu, K., et al. (2023). Annao Pingchong decoction alleviate the neurological impairment by attenuating neuroinflammation and apoptosis in intracerebral hemorrhage rats. J. Ethnopharmacol. *310*, 116298. https://doi.org/10.1016/j.jep.2023.116298.
54. Zhao, M., Wang, J., Xi, X., Tan, N., and Zhang, L. (2018). SNHG12 Promotes Angiogenesis Following Ischemic Stroke via Regulating miR-150/VEGF Pathway. Neuroscience *390*, 231–240. https://doi.org/10.1016/j.neuroscience.2018.08.029.
55. Al Mamun, A., Chauhan, A., Qi, S., Ngwa, C., Xu, Y., Sharmeen, R., Hazen, A.L., Li, J., Aronowski, J.A., McCullough, L.D., and Liu, F. (2020). Microglial IRF5-IRF4 regulatory axis regulates neuroinflammation after cerebral ischemia and impacts stroke outcomes. Proc. Natl. Acad. Sci. USA *117*, 1742–1752. https://doi.org/10.1073/pnas.1914742117.
56. Liu, L., Yuan, H., Yi, Y., Koellhoffer, E.C., Munshi, Y., Bu, F., Zhang, Y., Zhang, Z., McCullough, L.D., and Li, J. (2018). Ras-Related C3 Botulinum Toxin Substrate 1 Promotes Axonal Regeneration after Stroke in Mice. Transl. Stroke Res. *9*, 506–514. https://doi.org/10.1007/s12975-018-0611-5.

STAR★METHODS

KEY RESOURCES TABLE

REAGENT or RESOURCE	SOURCE	IDENTIFIER
Antibodies		
goat anti-CD31	R&D	Cat#FAB3628G-100
rabbit anti-Claudin5	Abcam	Cat#ab15106
rabbit anti-Occludin	CST	Cat#91131S
rabbit anti- ZO-1	Invitrogen	Cat#40-2200
rabbit anti-ZO-1	Proteintech	Cat#21773-1-AP
rabbit anti- MLCK	Abcam	Cat#ab76092
rabbit anti-p-MLC	CST	Cat#95777S
anti-rabbit Alexa Fluor 594	Abcam	Cat#ab150080
anti-rabbit Alexa Fluor 488	Abcam	Cat#ab150077
rabbit anti-β-actin	CST	Cat#4970
rabbit anti- MLCK	Abcam	Cat#ab76092
rabbit anti-MLC	Abcam	Cat#ab92721
rabbit anti-CaM	Abcam	Cat#ab45689
mouse anti-CaM	Abcam	Cat#ab2860
Protein A+G agarose beads	Beyotime	Cat#P2055
goat anti-rabbit IgG (H+L)	Elabscience	Lot E-AB-1003
goat anti-mouse IgG (H+L)	Elabscience	Lot E-AB-1001
Chemicals, peptides, and recombinant proteins		
Trifluoperazine	Solarbio	Lot 440-17-5
DMEM without glucose	Thermo Fisher Scientific	Lot 11966025
DMEM	Thermo Fisher Scientific	Lot 11965092
FBS	Inner Mongolia Opcel Biotechnology	Cat#BS-1105
Penicillin & Streptomycin	Thermo Fisher Scientific	Lot 15140122
Triphenyltetrazolium chloride	Solarbio	Lot IT0160
Evans blue dye	Sigma-Aldrich	Cat#E2129
FITC-dextran	Sigma-Aldrich	Cat#FD40S-100MG
Bovine serum albumin	Sigma-Aldrich	Lot 10711454001
RIPA lysis buffer	Sigma-Aldrich	Cat#20-188
Enhanced chemiluminescence reagents	MIKX	Lot MK-S500
RIPA buffer	Beyotime	Lot P0013B
Critical commercial assays		
BCA Protein Quantification Kit	Yeasen	Cat#20201ES76
Experimental models: Cell lines		
bEnd.3	Procell	Cat#CL-0598
Oligonucleotides		
Primers for qRT-PCR, see Table S1	This paper	N/A
Software and algorithms		
ImageJ	National Institutes of Health	N/A
SPSS v22.0	IBM	https://www.ibm.com/support/pages/spss-statistics-220-available-download
Zen 2	Zeiss	N/A

RESOURCE AVAILABILITY

Lead contact

Further information and requests for resources and reagents should be directed to and will be fulfilled by the lead contact, Mei Yuan (2012020002@usc.edu.cn).

Materials availability

This study did not generate new unique reagents.

Data and code availability

- All data reported in this paper will be shared by the lead contact upon request.
- This paper does not report original code.
- Any additional information required to reanalyze the data reported in this paper is available from the lead contact upon request.

EXPERIMENTAL MODEL AND STUDY PARTICIPANT DETAILS

Animals

The Ethics Committee for Scientific Research of the University of South China approved all the approaches used for breeding, caring for, and testing the experimental animals. We purchased wild-type (WT) C57BL/6J mice (age, 8–10 weeks; weight, 20–23 g) from SJA Laboratory Animal (Hunan, China). Since the female estrous cycle induces changes in estrogen levels that could cause changes in infarct size and neurological outcomes, this study used male mice only. Mice were housed in a temperature- and humidity-controlled animal facility with a 12-h light-dark cycle. Food and water were provided *ad libitum*. Animals were randomly assigned to the sham surgery, stroke, or post-stroke treatment groups. The core temperature of the mice was maintained at 37°C ± 0.5°C by using a heating pad throughout the experiment.

MCAO model mice and drug administration

Mice were anaesthetized (ketamine/xylazine/acepromazine, 50:5:1 mg/kg, i.p.) until they failed to respond to the tail-pinch test. A tethered thread with a silicon-coated tip was inserted into the common carotid artery, advanced to the origin of the MCA, and left in place. After 2 h of ischemia, reperfusion was achieved by removing the suture for 24 h. Rectal temperature was maintained at 37.0°C ± 0.5°C during the surgery by using a temperature-controlled heating pad. Sham-operated animals underwent exactly the same anesthesia and surgical procedures, except for the MCAO occlusion.[49] TFP (Solarbio, Beijing, China) was dissolved in normal saline and prepared at various concentrations. The TFP solution was administered intraperitoneally at doses of 2 mg/kg, 5 mg/kg, 10 mg/kg, and 20 mg/kg at 30 min before stroke induction and 1 h after stroke induction. The selection of the dosage and timing of administration was based on previous literature examining the effects of TFP in rodent models.[18,23,50]

Cell culture and reagents

The mouse brain endothelial cell (EC) line bEnd.3 was obtained from Procell (Wuhan, China). The bEnd.3 cells were cultured in Dulbecco modified Eagle medium (DMEM) supplemented with 10% fetal bovine serum (FBS; Inner Mongolia Opcel Biotechnology, Inner Mongolia, China), 1% penicillin, and 1% streptomycin (Thermo Fisher Scientific, Waltham, MA, USA) in a humidified incubator (at 37°C with 5% CO_2 and 95% air). The medium was changed every 2–3 days, and the cells were passaged no more than 3 times before use.

METHOD DETAILS

Measurement of infarct volume

Infarct volumes were calculated as described previously.[51] Mice were anaesthetized and sacrificed at 24 h after MCAO, and their brains were cut into 5 coronal sections (1 mm thick) and stained with 2% triphenyltetrazolium chloride (TTC; Solarbio, Beijing, China) for 20 min at 37°C. After fixation in 4% paraformaldehyde, the sections were photographed and analyzed using ImageJ software. Infarct volume was calculated as a percentage of the whole brain after correction for edema. The volume of the non-ischemic ipsilateral cerebral hemisphere was subtracted from the volume of the whole contralateral hemisphere to obtain the volume of the infarct, which was expressed as a percentage of the total volume of the contralateral hemisphere.

Evans blue dye assays

After I/R, the mice were injected via the tail vein with 0.1 mL of 2% Evans blue (EB; Sigma-Aldrich, St. Louis, MO, USA) or 0.1 mL of 2% fluorescein isothiocyanate (FITC)-dextran (MW: 40 kD; Sigma-Aldrich, St. Louis, MO, USA). The appearance of blue in the eyes and skin of the mice was observed after the EB/FITC injection. At 1 h after the injection, the mice were perfused with phosphate-buffered saline (PBS), and their brain tissues were harvested after the mice were euthanized with cervical dislocation. Fluorescence imaging was performed using a fluorescence microscope (Zeiss Apotome 2, JPN), and the images were analyzed and quantified using ImageJ software.[52]

Behavioral tests

The modified Neurological Severity Score (mNSS) was used as the behavioral test, which includes a comprehensive analysis of sensory function, motor function, autonomic dysreflexia, and balance. A normal score is 0, and higher scores reflect more severe neurological deficits.[53] The behavioral tests were conducted in a double-blind manner.

Oxygen-glucose deprivation and reoxygenation

We subjected bEnd.3 cells to oxygen-glucose deprivation (OGD), as previously described, to mimic the *in vivo* ischemic-hypoxic environment.[54] In brief, after being washed with warm glucose-free DMEM (Thermo Fisher Scientific, Waltham, MA, USA), the cells were transferred to an anaerobic chamber containing 94% N_2, 5% CO_2, and 1% O_2 at 37°C for 4 h. The cells were returned to normoxic culture conditions for 4 h for recovery. Some bEnd.3 cells that were treated identically, except for the OGD, served as a control group.[20]

In vitro trans-endothelial permeability assay

FITC-dextran was used to determine trans-endothelial permeability. First, bEnd.3 cells were seeded in the upper chamber of a 24-well Transwell chamber with a 0.4-μm filter insert (Corning, NY, USA). The cells were allowed to reach full confluence. After OGD, 40-kDa FITC-dextran (1 mg/mL; Sigma-Aldrich, St. Louis, MO, USA) was injected into the upper chamber. The fluorescence intensity was detected at 490 nm and 520 nm, by using Varioskan LUX (Thermo Fisher Scientific, Waltham, MA, USA) after 40 μL of the medium was removed from the lower chamber and shaken for 1 h. The negative control cells were treated with PBS, and the positive control cells were treated with FITC-dextran. The positive controls were initially added to the upper chamber. Trans-endothelial permeability was estimated by calculating the percentage of FITC-dextran transported into the lower chamber as follows: FITC-dextran transport (%) = (lower chamber medium fluorescence intensity − negative control)/positive control.

Lentiviral transfection

GENECHEM (Shanghai, China) generated a lentivirus overexpressing myosin light chain kinase (MLCK) by utilizing the GV341 vector. For the *in vitro* experiments, bEnd.3 cells were grown uniformly in 6-well culture plates, and used for transfection experiments when the cells grew to approximately 60%–80% confluence. For the *in vivo* experiments, the lentiviral vector was injected into the mouse brain as previously reported.[55,56] In brief, injections were administered at the following coordinates, which were located using a stereotaxic instrument: 0.5 mm anterior to the bregma, 2.0 or 3.0 mm lateral (right) to the sagittal suture, and 1.0 or 2.8 mm from the cranial surface. Concentrated lentivirus (0.5 μL total, $2*10^9$ transducing units/mL) was injected at the above sites at a rate of 0.5 μL/min. After the lentivirus injection, the needle was held in place for 5 min, and then slowly removed to allow the lentivirus to be well absorbed. At 4 weeks after the lentivirus microinjections, the mice were randomly assigned to the sham operation group or stroke model group.

Immunofluorescence assay

Tissue or cell samples were washed 3 times with PBS and then treated with 0.5% Triton X-100 in PBS for 30 min before being fixed in 5% bovine serum albumin (Sigma-Aldrich, St. Louis, MO, USA) in PBS for 1 h. Next, the samples were incubated with the primary antibodies at 4°C for 16–20 h. After being rinsed with PBS, the samples were incubated with the secondary antibodies at 37°C for 1 h. Finally, the samples were mounted using Fluoroshield™ (GeneTex Inc.) containing DAPI, and examined using fluorescence microscopy (Zeiss Apotome 2, JPN). Quantitative analysis was performed using ImageJ software.

We used the following primary antibodies and secondary antibodies at the indicated dilutions: goat anti-CD31 Alexa Fluor 488-conjugated antibody (1:400, R&D, Minneapolis, MN, USA), rabbit anti-Claudin-5 (1:100, Abcam, Cambridge, MA, USA), rabbit anti-Occludin (1:100, CST, Danvers, MA, USA), rabbit anti- zonula occludens (ZO)-1 (1:200, Invitrogen, Carlsbad, CA, USA), rabbit anti-MLCK (1:200, Abcam, Cambridge, MA, USA), rabbit anti-p-MLC (1:50, CST, Danvers, MA, USA), and anti-rabbit Alexa Fluor 488 or Alexa Fluor 594 (1:400, Abcam, Cambridge, MA, USA).

Western blotting

Total protein was extracted using radioimmunoprecipitation assay (RIPA) lysis buffer (Sigma-Aldrich, St. Louis, MO, USA) and quantified using the BCA Protein Quantification Kit (Yeasen, Shanghai, China). Equal quantities of protein from each sample were mixed with the loading buffer and boiled for 5 min. The final fractionation was performed using 10% sodium dodecyl sulfate-polyacrylamide gel electrophoresis (SDS-PAGE); then, the samples were transferred to polyvinylidene difluoride (PVDF) membranes (Millipore, Billerica, MA, USA) and subjected to SDS-PAGE splitting. Finally, the protein samples were validated using ChemiDoc XRS Plus (Bio-Rad, Hercules, CA, USA) and enhanced chemiluminescence reagents (MIKX, Shenzhen, China). The data obtained were validated using rabbit anti-CaM antibody (1:1000, Abcam, Cambridge, MA, USA), rabbit anti-Claudin-5 antibody (1:1000, Abcam, Cambridge, MA, USA), rabbit anti-Occludin antibody (1:1000, CST, Danvers, MA, USA), rabbit anti-ZO-1 antibody (1:1000, Invitrogen, Carlsbad, CA, USA), rabbit anti-MLCK antibody (1:1000, Proteintech, Wuhan, China), rabbit anti-MLC antibody (1:1000, Abcam, Cambridge, MA, USA), and rabbit anti-p-MLC antibody (1:1000, CST, Danvers, MA, USA). Protein loading was detected with rabbit anti-β-actin antibody (1:5000, CST, Danvers, MA, USA).

Co-immunoprecipitation assay

Mouse brain tissue was harvested, lysed in RIPA buffer (Beyotime, Shanghai, China), and quantified using the BCA Protein Assay Kit (Thermo Fisher Scientific, Waltham, MA, USA). Next, 1 mg total protein extract was incubated with 2 μg mouse anti-CaM antibody (1:200, Abcam,

Cambridge, MA, USA) at 4°C for 12–16 h. The mixture was then incubated with protein A+G agarose beads (Beyotime, Shanghai, China) for 4 h, washed at least 4 times with PBS, and boiled in SDS sample buffer (Haoran Bio, Shanghai, China) for 5 min. The protein samples were separated using 10% SDS-PAGE gels and transferred to PVDF membranes (MilliporeSigma, Burlington, MA, USA). For co-immunoprecipitation, the PVDF membranes were incubated overnight with rabbit anti-MLCK antibody (1:1000, Proteintech, Wuhan, China) at 4°C, and then, the blots were incubated with goat anti-rabbit IgG (H+L) and goat anti-mouse IgG (H+L) (1:5000, Elabscience, Wuhan, China) after being rinsed with TBST, for 1 h at ambient temperature.

Quantitative real-time polymerase chain reaction assay

Total RNA was extracted from tissues and cells by using Trizol reagent (Invitrogen, Carlsbad, CA, USA). Reverse transcription was performed using the GoScript™ Reverse Transcription System Reverse Transcription Kit (Promega, Madison, WI, USA). The GoScript™ qPCR Master Mix Kit (Promega, Madison, WI, USA) was used for fluorescence real-time quantitative polymerase chain reaction (RT-qPCR) assays, according to the manufacturer's instructions. Gene expression was calculated using the 2-ΔΔCT method with GAPDH as an internal reference. Table S1 shows the sequences of the primers used for qRT-PCR.

QUANTIFICATION AND STATISTICAL ANALYSIS

All experimental data were analyzed using SPSS *v*22.0 statistical analysis software. Data were expressed as mean ± standard error of mean. Independent-samples *t*-tests were used for comparisons between 2 groups. Paired-samples *t*-tests were used for comparisons between pre- and post-treatment values. One- or two-way analysis of variance (ANOVA) with the Tukey post-hoc test was used to analyze differences between 3 or more groups or between groups over time. Statistical significance was defined as $P < 0.05$. Data are represented as mean ± SEM. ns, $P > 0.05$, $*P < 0.05$, $**P < 0.01$.